JWST/NIRCam Narrowband Survey of Paβ Emitters in the Spiderweb Protocluster at $z = 2.16$

Rhythm Shimakawa[1,2] , J. M. Pérez-Martínez[3,4] , Helmut Dannerbauer[3,4] , Yusei Koyama[5] , Tadayuki Kodama[6] ,
Pablo G. Pérez-González[7] , Chiara D'Eugenio[3,4] , Yuheng Zhang[3,4,8,9] , Abdurrahman Naufal[10,11] , and Kazuki Daikuhara[6]

[1] Waseda Institute for Advanced Study (WIAS), Waseda University, 1-21-1, Nishi-Waseda, Shinjuku, Tokyo, 169-0051, Japan; rhythm.shimakawa@aoni.waseda.jp
[2] Center for Data Science, Waseda University, 1-6-1, Nishi-Waseda, Shinjuku, Tokyo, 169-0051, Japan
[3] Instituto de Astrofísica de Canarias, E-38205 La Laguna, Tenerife, Spain
[4] Universidad de La Laguna, Dpto. Astrofísica, E-38206 La Laguna, Tenerife, Spain
[5] Subaru Telescope, National Astronomical Observatory of Japan, National Institutes of Natural Sciences 650 North A'ohoku Place, Hilo, HI 96720, USA
[6] Astronomical Institute, Tohoku University, 6-3, Aramaki, Aoba, Sendai, Miyagi 980-8578, Japan
[7] Centro de Astrobiología (CAB), CSIC-INTA, Ctra. de Ajalvir km 4, Torrejón de Ardoz, E-28850, Madrid, Spain
[8] Purple Mountain Observatory, Chinese Academy of Sciences, 10 Yuanhua Road, Nanjing, 210023, People's Republic of China
[9] School of Astronomy and Space Science, University of Science and Technology of China, Hefei, Anhui 230026, People's Republic of China
[10] Department of Astronomical Science, The Graduate University for Advanced Studies, 2-21-1 Osawa, Mitaka, Tokyo 181-8588, Japan
[11] National Astronomical Observatory of Japan, 2-21-1 Osawa, Mitaka, Tokyo 181-8588, Japan

Abstract

We report the initial result of our Paβ narrowband imaging on a protocluster with the JWST Near Infrared Camera (NIRCam). As NIRCam enables deep narrowband imaging of rest-frame near-infrared lines at $z > 1$, we target one of the most studied protoclusters, the Spiderweb protocluster at $z = 2.16$, in which previous studies have confirmed more than a hundred member galaxies. The NIRCam F405N narrowband filter covers in the Paβ line the protocluster redshift given by known protocluster members, allowing for the search for new member candidates. The weight-corrected color–magnitude diagram obtained 57 sources showing narrowband excesses, 41 of which satisfy further color selection criteria for limiting the sample to Paβ emitter candidates at $z \sim 2.16$, and 24 of them do not have Hα emitter counterparts. The Paβ emitter candidates appear to follow the spatial distribution of known protocluster members; however, follow-up spectroscopic confirmation is required. Only 17 out of 58 known Hα-emitting cluster members are selected as Paβ emitters in the current data, albeit the rest fall out of the narrowband selection owing to their small Paβ equivalent widths. We derive the Paβ luminosity function in the Spiderweb protocluster, showing a normalization density of $\log \phi^* = -2.53 \pm 0.15$ at a characteristic Paβ luminosity of $\log L^* = 42.33 \pm 0.17$. Furthermore, we examine the possibility of detecting faint line emitters visible only in the narrowband image but find no promising candidates.

Unified Astronomy Thesaurus concepts: Protoclusters (1297); High-redshift galaxy clusters (2007); Emission line galaxies (459); Near infrared astronomy (1093); Galaxy formation (595); Galaxy evolution (594)

Materials only available in the online version of record: machine-readable table

1. Introduction

Exploring various galaxy populations and uncovering their physical properties through multiwavelengths across large-scale structures and cosmic time lead to a greater understanding of the diverse growth histories of galaxies and how environmental effects shape the galaxy assembly. As reviewed by, e.g., A. E. Shapley (2011), C. Conroy (2013), C. L. Carilli & F. Walter (2013), N. M. Förster Schreiber & S. Wuyts (2020), and L. J. Tacconi et al. (2020), a great deal of deep and high-resolution observations have been conducted for galaxies in the distant Universe. However, until recent years, we had lacked such high-quality data of the rest-frame near-infrared (NIR) emissions in high-redshift galaxies owing to the absence of suitable instruments, and thus they were limited to galaxies at $z \lesssim 1.5$ (e.g., A. Alonso-Herrero et al. 2006; D. Calzetti et al. 2007; A. Calabrò et al. 2019; C. Gimenez-Arteaga et al. 2022), except in the case of lensed galaxies (C. Papovich et al. 2009). Nevertheless, it is essential to investigate galaxies, particularly

at $z = 2$–4, as during this redshift interval, known as the cosmic noon, the Universe reached the peak epoch of cosmic star formation rate density across cosmic time (P. Madau et al. 1998; S. J. Lilly et al. 1999).

With the advent of the James Webb Space Telescope (JWST), this situation has changed drastically; its powerful NIR instruments enable unprecedented depth in the rest-frame NIR observation for galaxies at $z = 1$–3, with a spatial resolution of only $\sim 0.\!''1$ for the first time. A noteworthy aspect of the observational capabilities is the equipment with four narrowband (NB) filters (F323N/F405N/F466N/F470N) on the Near Infrared Camera (NIRCam; M. J. Rieke et al. 2005), enabling deep NB mapping of Paα (or Paβ) lines at redshifts of 0.73/1.16/1.48/1.51 (or 1.52/2.16/2.63/2.67), respectively. As Paschen lines are located in the NIR regime, they can be taken as nearly unbiased tracers of current star formation (R. C. J. Kennicutt 1998; D. Calzetti et al. 2007). Indeed, new studies have begun investigating Pashcen lines of galaxies at $z > 1$ with JWST. For instance, C. Neufeld et al. (2024) have revisited the star-forming main sequence using Paα line and rest-frame NIR photometry, which shows that its scatter of ~ 0.29 dex is consistent with those of previous studies based on the rest-frame optical lines or spectral energy

distribution (SED) fitting. N. A. Reddy et al. (2023) have suggested the possible presence of star formation not captured by Balmer lines, exemplifying the scientific importance of Paschen line observations.

One of the NIRCam NB filters can cover Paβ lines of galaxies in one of the most studied galaxy protoclusters, the Spiderweb protocluster (C. L. Carilli et al. 1997; J. D. Kurk et al. 2000; L. Pentericci et al. 1997, 2000), associated with the Spiderweb radio galaxy, PKS 1138−262 at $z = 2.16$ (J. G. Bolton et al. 1979; H. J. A. Roettgering et al. 1994, 1997; R. van Ojik 1995). Beginning with the first discovery of significant overdensity of Lyα emitters (J. D. Kurk et al. 2000; L. Pentericci et al. 2000), more than a hundred protocluster member galaxies have now been identified across various wavelength regimes (e.g., J. D. Kurk et al. 2004a, 2004b; S. Croft et al. 2005; M. Doherty et al. 2010; M. Tanaka et al. 2010, 2013; Y. Koyama et al. 2013a; R. Shimakawa et al. 2014, 2018b; S. Jin et al. 2021; J. M. Pérez-Martínez et al. 2023, and see, e.g., R. Shimakawa et al. 2018b; P. Tozzi et al. 2022b for overviews of previous surveys). The protocluster core has recently been confirmed by the thermal Sunyaev–Zel'dovich effect (L. Di Mascolo et al. 2023). They report that the halo mass is estimated to be $M_{500} = 3.46 \times 10^{13}$ $M_\odot$, representing progenitors of galaxy clusters with $M_{500} = (5.6–8.8) \times 10^{14}$ $M_\odot$ at $z = 0$ (see also R. Shimakawa et al. 2014; P. Tozzi et al. 2022a; M. Lepore et al. 2024). M. Lepore et al. (2024) measured a temperature profile inside the protocluster core for the first time and then suggested the presence of a strong cool flow with 250–1000 $M_\odot$ yr^{-1} and an energy budget of ongoing feedback power beyond $\sim 10^{43}$ erg s^{-1}, which is primarily driven by the radio galaxy. In fact, the abrupt changes owing to the synergistic effect of gas feeding and feedback mechanisms are expected in protocluster halos in this period, according to cosmological simulations, such as cold streams in hot halos (A. Dekel et al. 2009; J. Suresh et al. 2019; J. Stern et al. 2020) and preheating driven by active galactic nuclei (AGN) feedback (G. W. Pratt et al. 2010; A. Chaudhuri et al. 2013; A. Iqbal et al. 2017; R. Kooistra et al. 2022). These observations and simulations all suggest that the Spiderweb protocluster is rapidly transitioning to the bona fide cluster. Hence, it provides important insights into galaxy cluster formation.

Motivated by such backgrounds, we conduct Paβ NB imaging toward the Spiderweb protocluster with JWST/ NIRCam (Cycle 1 GO 1572, P.I. Dannerbauer and Koyama). The deep NB (F405N) data provide us with a new window to search for star-forming galaxies and AGNs in the Paβ line at $\lambda = 1.28$ μm in the Spiderweb protocluster. Therefore, the main scope of this study, as part of a series of early reports with J. M. Pérez-Martínez et al. (2024), is to explore this classic protocluster from yet another perspective of the Paβ line and to offer unique member candidates. This paper is organized as follows: we first summarize the NIRCam data set (Section 2), then we demonstrate the NB technique and color–color selection for selecting candidates of protocluster members (Section 3). Here, we utilize the archival Hα emitters (HAEs) from R. Shimakawa et al. (2018b, 2024a) for the purpose of validation. Subsequently, we discuss the spatial distribution of the obtained candidates of Paβ emitters associated with the Spiderweb protocluster, and measure the Paβ luminosity function in the survey field (Section 4). We also discuss the possible detection of emission-line-dominated candidates
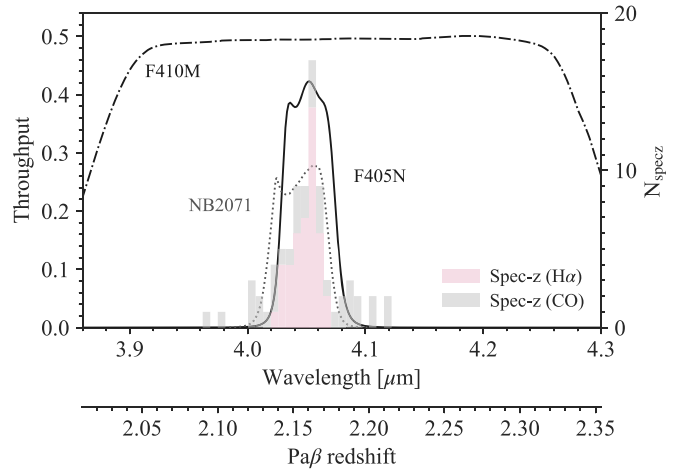
Figure 1. Filter response curves and redshift distribution of spectroscopically confirmed members in the Spiderweb protocluster. The dotted, solid, and dashed–dotted lines indicate the filter throughput of the MOIRCS/NB2071, NIRCam/F405N, and F410M bands, respectively. Spectroscopic confirmations with Hα and CO(1–0) lines are shown separately by pink and gray (e.g., R. Shimakawa et al. 2014; S. Jin et al. 2021; J. M. Pérez-Martínez et al. 2023).

detected only in the NB image. Finally, we summarize the entire flow of the paper and the obtained results in Section 5.

We assume a flat lambda cold dark matter model with $h = 0.693$ and $\Omega_M = 0.286$, consistent with those obtained from the WMAP nine-year data (G. Hinshaw et al. 2013). We use the G. Chabrier (2003) stellar initial mass function and the AB magnitude system (J. B. Oke & J. E. Gunn 1983). We assume a positive equivalent width (EW) for emission lines unless otherwise noted.

2. Data and Sample

2.1. NIRCam Imaging

2.1.1. Observation

We conduct NB imaging on the Spiderweb protocluster (Cycle1 GO 1572; P.I. Dannerbauer and Koyama) with the F405N and F410M filters (in parallel, F115W and F182M filters on the blue channel) on NIRCam (M. J. Rieke et al. 2005). The NIRCam F405N filter ($\lambda_{\text{center}} = 4.055$ μm, FWHM = 0.046 μm) covers a Paβ redshift range of $z = 2.165 \pm 0.018$, which covers well the protocluster redshift and largely overlaps the redshift coverage of $z = 2.156 \pm 0.025$ by the previous Hα imaging (Figure 1). The spatial resolution of $0.''14$ in FWHM in the F405N band is comparable to those of the Hubble Space Telescope (HST) Advanced Camera for Surveys (ACS; FWHM = $0.''11$; e.g., J. A. Stevens et al. 2003) and Atacama Large Millimeter/submillimeter Array Band-7 data (FWHM = $0.''16$; Y. Koyama et al. 2024, in preparation). Additionally, the NIRCam F405N filter pairs with our companion filter, NB2071, installed on the Multi-Object Infrared Camera and Spectrograph (MOIRCS) on the Subaru Telescope (T. Ichikawa et al. 2006; R. Suzuki et al. 2008), allowing us to analyze Paβ lines of the existing Hα emitters in the Spiderweb protocluster (Y. Koyama et al. 2013a; R. Shimakawa et al. 2018b), as reported in the companion paper (J. M. Pérez-Martínez et al. 2024).

In the observing run, we set a primary dither pattern of FULLBOX 4TIGHT of ROWS×2 with 35% overlap and COLUMNS=1 with 10% overlap, which can cover the $3' \times 6'$ square field around the Spiderweb galaxy, which amounts to
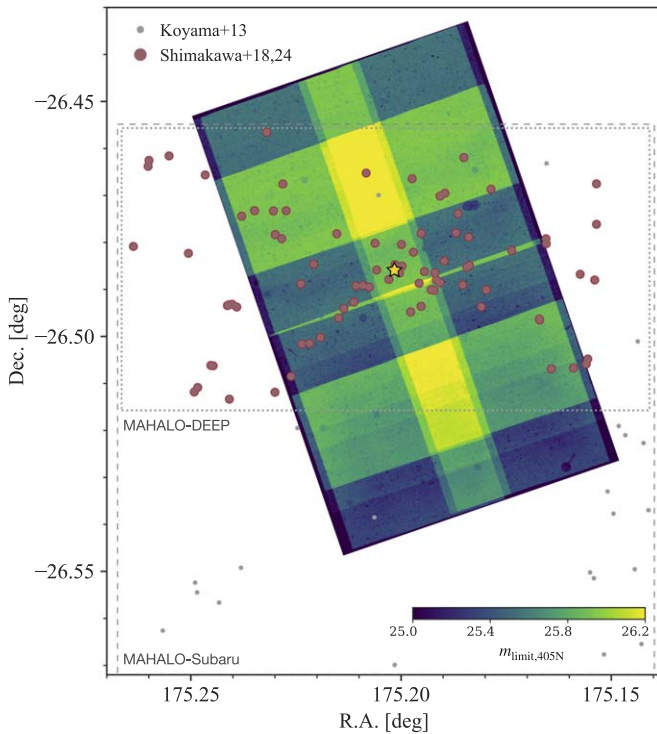
Figure 2. Spatial distribution of known HAEs from previous NB imaging. The red circles show the HAE samples in the deep field depicted by the dotted square (MAHALO-DEEP; R. Shimakawa et al. 2018b, 2024a), and the gray dots indicate additional HAEs from the original NB imaging covering two times wider as depicted by the dashed square (MAHALO-Subaru; Y. Koyama et al. 2013a). The yellow star indicates the Spiderweb radio galaxy. The color map corresponds to the imaging depth of the F405N image.

the total number of exposures $N_{exp} = 2-8$ per field (Figure 2). The FULLBOX TIGHT dither is adopted to maximize the observing efficiency. The maximum integrations reach 63 minutes in the F405N and F115W bands and 21 minutes in the F410M and F182M bands. Also, the position angle is not fixed to allow for greater flexibility in the observing schedule. Approximately 60% of the survey area is covered by the Hα NB imaging with Subaru/MOIRCS (Y. Koyama et al. 2013a; R. Shimakawa et al. 2018b) and the wide CO (1−0) emitter survey with ATCA (S. Jin et al. 2021). In this work, we employ only Hα (+ [N II])-emitting galaxies from R. Shimakawa et al. (2018b), whose sky coordinates are available in R. Shimakawa et al. (2024a). Of these, 58 HAEs are covered by the NIRCam survey area (Figure 2), and thus, they can be used to select Paβ emitter candidates in this work, as shown in Section 3.

2.1.2. Data Reduction

The raw frames are downloaded from the Barbara A. Mikulski Archive for Space Telescopes at doi:10.17909/vx25-q902, processed by Science Data Processing version 2023-1a, and post-processed with the JWST Science Calibration pipeline version 1.10.2 under the Calibration Reference Data System context 1140.pmap (H. Bushouse et al. 2023). Apart from the three official pipeline stages, we carry out several offline procedures to improve the calibration using the Rainbow JWST pipeline, described in P. G. Pérez-González et al. (2024). In particular, $1/f$ noise[12] is removed, and the background is

homogenized with a combination of row/column and box-median filtering. In both cases, sources are masked before the procedure using a mask produced with a dry run of the official pipeline, including a mask dilation, and by-hand masking of the brightest, most extended sources in the cluster (and some bright stars).

The final mosaics are built with a 0″.03 pixel scale, and their imaging qualities are evaluated in Section 2.2. The World Coordinate System is calibrated using the TWEAKREG patch developed by the CEERS collaboration (M. B. Bagley et al. 2023) using as reference for the JWST data the F410M image (the deepest one), and then aligning this frame to the HST/ACS F814W image (G. K. Miley et al. 2006). For this task, we create a catalog containing sources within the overlapping area between the JWST and HST filters. We request our sources to fulfill a signal-to-noise ratio of $S/N > 10$ per pixel within a minimum area equivalent to twice the size of the point-spread function (PSF) in the respective filters and remove objects with significant elongations or distortions which could introduce additional uncertainties in the determination of their positions.
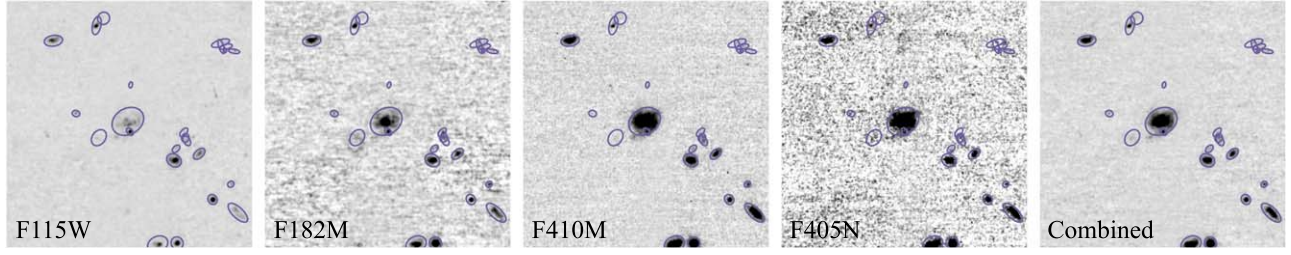
2.2. Source Detection

We conduct source detection and noise estimation based on the final mosaic images. These tasks have to be done carefully because the imaging depth is not homogeneous across the survey field (Figure 2). In addition to the different number of exposures ($N_{exp} = 2-8$), many dips of the imaging depth exist in the fields even with the same net integration, owing to the sensitivity variance between detectors and within individual detectors. These factors significantly affect the noise estimations, and hence the NB selection as described in the following (Section 3). We are also concerned about a flux loss in the galaxy outskirts because diffuse components may be missed on the NIRCam images, especially in the F450N band, which is relatively shallower compared to the other medium or broad bands. This may cause serious underestimations of Kron radii when measuring total flux densities. Besides, the NIRCam data reduction pipeline still needs to be improved as it leaves some artifacts, such as snowballs, due to the impacts of cosmic rays,[13] critical for NB imaging requiring long exposure per frame. Such artifacts may be present as false NB emitters (NBEs) if we do not clear them adequately (see also Section 4.3).

Considering various concerns raised above, we adopt a median combined image of all four available bands (F115W + F182M + F410M + F405N) for the source extraction (Figure 3), enabling us to minimize the aforementioned issues that may happen when only the NB image is used. For instance, the cosmic ray effect can be mitigated in the median-stacked image, and its deeper imaging depth helps us determine the Kron radius relatively well, as we can reduce the risk of overlooking diffuse components. Instead, this decision causes another potential issue of ignoring emission-line-dominated objects (so-called NB-only emitters), visible only in the NB image but not in the other bands (see, e.g., M. Hayashi et al. 2016; R. Shimakawa et al. 2018a). However, determining whether such faint-end sources are real or not (e.g., noise and artifact) is challenging, given the current limitations of the JWST/NIRCam data reduction tool. Therefore, these peculiar objects are discussed briefly in Section 4.3.

---

[12] https://jwst-docs.stsci.edu/known-issues-with-jwst-data/nircam-known-issues

[13] https://jwst-docs.stsci.edu/data-artifacts-and-features/snowballs-and-shower-artifacts

Figure 3. Example cutout images with 0.3×0.3 arcmin^2. From left to right, panels show the F115W, F182M, F410M, and F405N band images, and the four-band combined image, respectively, on the same flux scale in counts. Here, the F115W and F182M images are smoothed by the Gaussian kernels to match their resolutions to the F410M and F405N images. The magenta circles indicate the Kron radius obtained from the combined image for each detection.

Cutout examples of reduced images can be found in Figure 3. We combine all four available band images in the median after aligning their pixel coordinates and point source FWHMs. Figure 4 indicates radial profiles of composite images of 17-point sources in the four bands, showing that their radial profiles agree well with each other. Notably, we have selected only faint point sources that are not saturated in the F115W band. Note that PSF wings do not affect the NB selection as they are beyond the aperture radius of $0\rlap{.}''15$ or 5 pixels (Section 3.1). In Figure 4, the point sources have been extracted at the forced pixel coordinates for all the imaging data. Therefore, the consistent radial profiles also indicate that their pixel coordinates are overall consistent with each other on the subpixel scale. Then, we perform source detection using SEXTRACTOR (version 2.19.5, E. Bertin & S. Arnouts 1996) with detection parameters of DETECT_MINAREA = 25, DETECT_THRESH = 1.5, ANALYSIS_THRESH = 1.5, where we have determined these parameters through trial and error to avoid detecting visible artifacts. We use default deblending parameters in DEBLEND_NTHRESH = 32 and DEBLEND_MINCONT = 0.005. After manually masking bright stars and their diffraction spikes, we run the source extractor in the dual imaging mode, weighting through a weight map of the combined image. Consequently, 16,444 sources are detected, including noisy objects. Examples of source detection and their obtained Kron radii in each image can be found in Figure 3.

We employ a commonly used technique for noise estimation based on random aperture photometry but with various aperture diameters while measuring the mean weight values within the aperture areas. We then obtain the best-fit error functions, $\sigma(D, W)$, given circularized diameter and weight values using the PHOTUTILS package (version 1.10.0, L. Bradley et al. 2023), enabling the estimation of photometric errors for all detected sources. Here, D is a circularized aperture diameter ($D = 0\rlap{.}''3$ is applied in the NB selection), and W is the mean weight value within a corresponding aperture area in the weight map. We distribute empty apertures ($N \sim 30{,}000$ in each radius) with $0\rlap{.}''15$–$1\rlap{.}''20$ radii variable by $0\rlap{.}''15$ on blank fields in each image. We then derived limiting magnitudes and the best-fit functions in the four NIRCam imaging data (Figure 5). Consequently, we confirm that the sky errors decrease with the square root of weight values, $W_{\mathrm{band}}^{-0.5}$, which is natural by definition. They also increase with increasing aperture diameter by $D^{\sim 1.4}$ owing to partial pixel-to-pixel correlations. The obtained error function in each band can be described as follows:

$$\sigma(D, W)_{\mathrm{F115W}} = 15.760 \, W_{\mathrm{F115W}}^{-0.5} \times (D/5)^{1.501}, \quad (1)$$

$$\sigma(D, W)_{\mathrm{F182M}} = 9.825 \, W_{\mathrm{F182M}}^{-0.5} \times (D/5)^{1.292}, \quad (2)$$

$$\sigma(D, W)_{\mathrm{F410M}} = 14.874 \, W_{\mathrm{F410M}}^{-0.5} \times (D/5)^{1.408}, \quad (3)$$
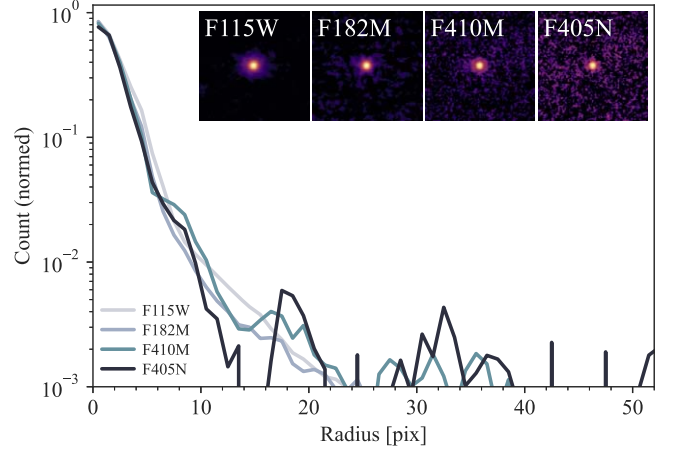
Figure 4. Radial profiles of composite point sources in the four photometric bands. The pixel scale is $0\rlap{.}''03$. In order from the lightest color, the curves show those in the F115W, F182M, F410M, and F405N bands, respectively. Their composite images are inset in the upper right. We selected only 17 faint point sources at the forced positions based on the combined image because most of the point sources are saturated in the F115W band.

$$\sigma(D, W)_{\mathrm{F405N}} = 22.509 \, W_{\mathrm{F405N}}^{-0.5} \times (D/5)^{1.380}. \quad (4)$$

Uncertainties of flux densities in fixed aperture and Kron photometry for each source are estimated based on these prescriptions throughout the study by adopting their circularized diameters. Five sigma limiting magnitudes in Figure 5 are derived through $m_{\mathrm{limit}} \equiv \mathrm{ZP} - 2.5 \log(5\sigma(D, W))$, where ZP is the zero-point magnitude. We adopt a zero-point magnitude of 28.065 mag for all bands except for the NB (F405N) image, including a small zero-point correction of $+0.03$ mag to fit a zero-point offset ($=0.00$ mag) between F410M and F405N (see also Section 3.2). For the obtained images, their limiting magnitudes are consistent with those expected from the JWST Exposure Time Calculator (K. M. Pontoppidan et al. 2016). However, the different net integrations (up to ~ 0.75 mag given $N_{\mathrm{exp}} = 2{-}8$) and sensitivity variances within individual detectors lead to the differential of imaging depths up to $\sim$one mag, depending on the source position.

3. Narrowband Selection

3.1. Color–Magnitude Selection

To search for Paβ emitter (PBE) candidates at $z \sim 2.16$, we perform NB selection similarly to previous approaches (e.g., A. J. Bunker et al. 1995; D. Sobral et al. 2009, 2013; M. Hayashi et al. 2010; J. Matthee et al. 2017; R. Shimakawa et al. 2018a)
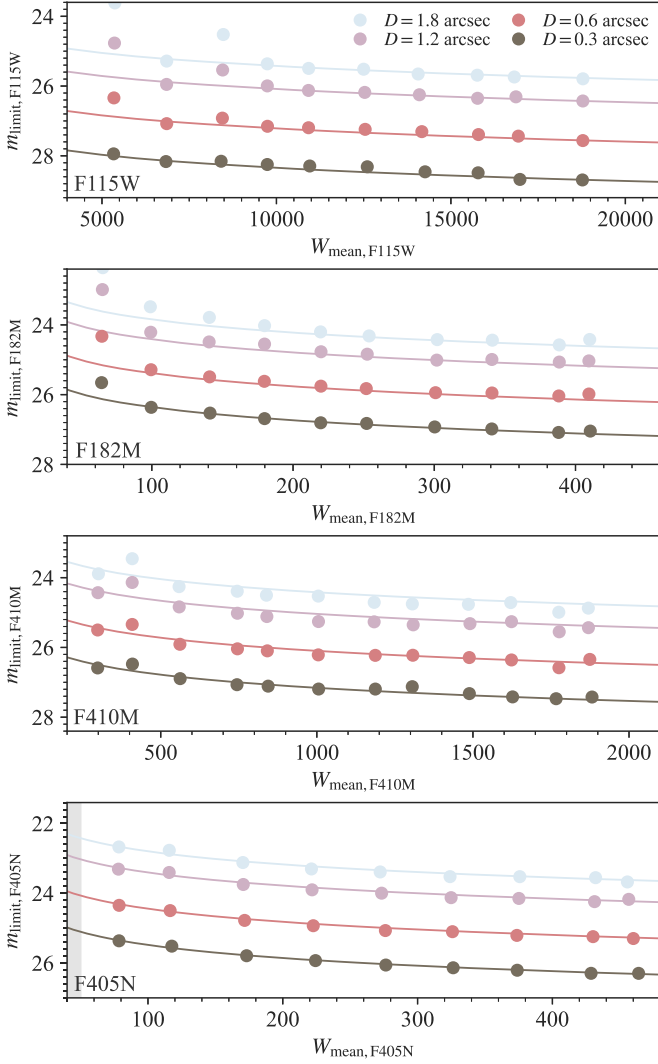
Figure 5. Limiting magnitude (5σ) as a function of the mean weight value in different aperture diameters. From the top, each panel shows the limiting magnitude in the F115W, F182M, F410M, and F405N bands, respectively. The black, red, magenta, and cyan circles show some cases of derived limiting magnitudes in aperture diameters of 0″3, 0″9, 1″2, and 1″8, respectively, and their best-fit error functions are depicted by corresponding color curves (Equations (1)–(4)). We mask noisy edges in the F405N image in the source extraction, shown by the gray-filled area in the bottom panel.

as the following prescriptions:

$$BB - NB > -2.5 \log(1 - \Sigma\delta 10^{-0.4(ZP-NB)}), \quad (5)$$

$$BB - NB > 0.124, \quad (6)$$

where Σ is a sigma confidence level ($\Sigma = 3$ is adopted in this work) of NB (F405N) excess relative to F410M in fixed aperture photometry of 0″3 diameter, and δ represents the combined 1σ background noise in the NB (F405N) and BB (F410M) bands, defined by $\delta^2 = \sigma(D, W)_{NB}^2 + \sigma(D, W)_{BB}^2$ (see Equations (3)–(4)). The latter color threshold (Equation (6)) is a selection cut for the EW limit in the NB flux (=20 Å in the rest frame at $z = 2.16$), which is comparable to previous NB surveys.

We perform NB selection based on the obtained noise functions, as described in Section 2.2. The resultant color–magnitude diagram is represented in Figure 6, where we plot 6384 sources detected in the F410M band at greater than 2σ levels. The typical flux limit ($\Sigma = 3$) corresponds to
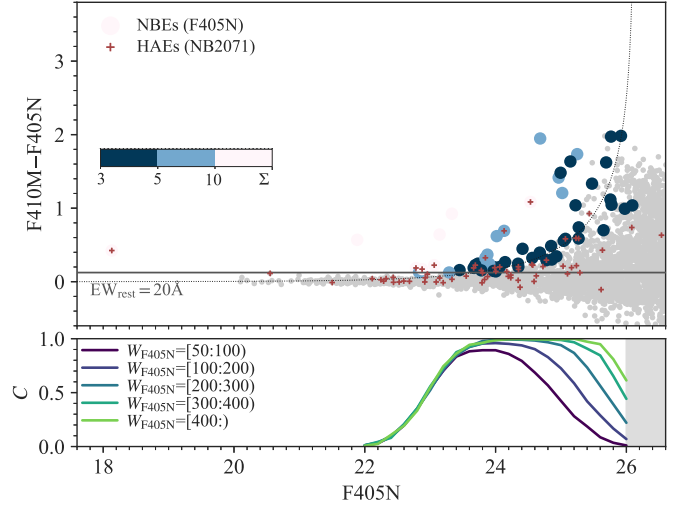
Figure 6. Top: color–magnitude diagram for the NBE selection (see Equations (5)–(6)). The gray dots show all sources in the F405N band, and the colored circles represent the emitter candidates above 3σ confidence levels, where symbol colors indicate significance levels of the NB excess (see the color bar), and the mean color threshold is depicted by the dotted curve. The red dots mark known HAEs (R. Shimakawa et al. 2024a, Table A). The black horizontal line depicts the EW cut (=20 Å in the rest frame). Bottom: selection completeness, C (recovery rate of mock NBEs) as a function of F405N (see Section 3.1 for more details). Line colors indicate the completeness in different weight values (from the darker color, $W_{F405N} = $ [50:100], [100:200], [200:300], [300:400], [400:], where higher weights mean deeper as in Equation (4) and Figure 5.

$\sim 2 \times 10^{-18}$ erg s^{-1} cm^{-2}. As expected, this is comparable with the Hα+[NII] flux limit of $\sim 3 \times 10^{-17}$ erg s^{-1} cm^{-2} in our previous NB imaging with Subaru/MOIRCS (R. Shimakawa et al. 2018b), given the dust-free line ratio of Hα/Paβ = 17.5 in the case B recombination (V. Luridiana et al. 2015). After careful visual confirmation, we obtained 57 emitter candidates showing color excesses above $\Sigma = 3$ (Equation (5)) and the rest-frame EW > 20 Å (Equation (6)), 17 of which are successfully matched to the known HAEs within 0″5 (R. Shimakawa et al. 2018b).

Notably, although most known HAEs are expected to have sufficiently bright Paβ line fluxes, only 17 out of 58 HAEs show significant NB excesses in the F405N band (Figure 6). We confirm that this trend is particularly evident in the massive end with $M_\star > 4 \times 10^{10} M_\odot$ (R. Shimakawa et al. 2024a, Table A1), where only the Spiderweb radio galaxy meets the selection criteria (1/13). The major reason for missing HAEs in Paβ lines is a selection bias due to the small aperture diameter of 0″3 and the EW cut adopted for the selection. This aperture size has been set to maximize the NIRCam's great sensitivity to compact objects and minimize the effects of nearby cosmic ray pixels; however, it can track only central regions within a 1.27 kpc radius and cannot trace outer star formation. Thus, massive star-forming galaxies forming central bulges cannot be trapped by the NB selection due to the relatively small EWs in the galaxy centers. Indeed, the forthcoming paper (R. Shimakawa et al. 2024b) confirms the typical rest-frame $EW_{Pa\beta} \sim 10$ Å of such massive HAEs in the aperture area, which is lower than the selection threshold of 20 Å, according to the composite image of massive HAEs with $M_\star > 2 \times 10^{10} M_\odot$. Line flux ratios for individual HAEs are examined in detail by J. M. Pérez-Martínez et al. (2024).

Furthermore, we examine the recovery rates of the NB selection through a Monte Carlo simulation similar to previous

studies (D. Sobral et al. 2009, 2013; R. Shimakawa et al. 2018a). The calculation is performed as follows. First, 200 PSF images made from composite images of point sources are embedded at random positions in the F405N and F410M images. Here, for a given F405N magnitude, F410M magnitudes are determined following a regression line between F405N and F410M for the selected NBEs, with a scatter of 0.1 mag in view of color (EW) variations. We run 50 iterations in the Monte Carlo simulation for a given F405N magnitude in a step of 0.2 mag at 22–26 mag; hence, 10,000 point sources are embedded in each magnitude bin. We then evaluate the recovery rate (known as selection completeness, C) by applying NB selection (Equations (5)–(6)) for the embedded sources. The obtained selection completeness is summarized in Figure 6, which plots completeness values in different weight intervals considering the imaging depth variation. It shows that there is a significant variance of the selection completeness depending on the source location: the completeness still reaches approximately 60% at the faint end if the source is located in the deepest region ($W_{F405N} \geqslant 400$) while dropping to almost zero in the shallow regions ($W_{F405N} < 200$). We can also see that the selection completeness decreases toward the bright end (F405N $<$ 23 mag), regardless of weight values, owing to lower EWs of NBEs. We adopt the obtained completeness values when measuring the Paβ luminosity function in Section 4.2.

3.2. Color–Color Selection

This section examines which emission lines may affect our NB selection, and then tries to select more plausible candidates associated with the Spiderweb protocluster using color–color selection. Even though the selected NBEs are more likely to be Pa $\beta\lambda12822$ emitters at $z = 2.2$ compared with those in the random field because of their significant overdensities (e.g., R. Shimakawa et al. 2018b, $\delta \sim 10$); various strong emission lines at different redshifts may contribute to the emitter sample. Specifically, we may have line emitter contaminants, such as PAH $\lambda3.3\,\mu m$ at $z = 0.2$ or Paα at $z = 1.2$ in the foreground, and Hα at $z = 5.2$ or [O III] doublet at $z \sim 7.1$ in the background.

Figure 7 demonstrates which emission lines significantly impact NB excess (F410M−F405N) depending on the source redshift, based on SED templates of star-forming and quiescent galaxies from a program termed Easy and Accurate Redshifts from Yale (EASY; G. B. Brammer et al. 2008). We adopt a set of 12 standard templates (tweak_fsps_QSF_12_v3) from available models in the software program, showing that PAH $\lambda3.3\,\mu$m at $z = 0.2$, Pa $\alpha\lambda18756$ at $z = 1.2$, [S III]$\lambda\lambda$ 9071,9533 doublet at $z \sim 3.3$, H$\alpha\lambda6565$ at $z = 5.2$, or [O III] $\lambda4960,5008$ doublet at $z \sim 7.1$, would greatly contribute to the NB selection. It should be noted here that NB excesses vary more widely with galaxy properties than indicated in the figure (e.g., D. Sobral et al. 2013). Indeed, most confirmed PBEs with HAE counterparts show higher NB excesses (EW $\gtrsim 100$ Å) than the model templates. On the other hand, for those with very high NB excess (>1.4 mag or EW $\gtrsim 2000$ Å in Figure 6), it seems likely that they are emitters other than PBEs, e.g., Hα emitters at $z = 5.2$ given the redshift evolution of EW$_{H\alpha}$ (~ 3700 Å at $z = 5.2$ according to P. Rinaldi et al. 2023, Figure 11). However, we stress that 7 of 8 NBEs with such high NB excesses (>1.4 mag) are excluded by the color–color selection in the following. Figure 7 also shows that these emission-line contributions are expected to occur solely in star-forming
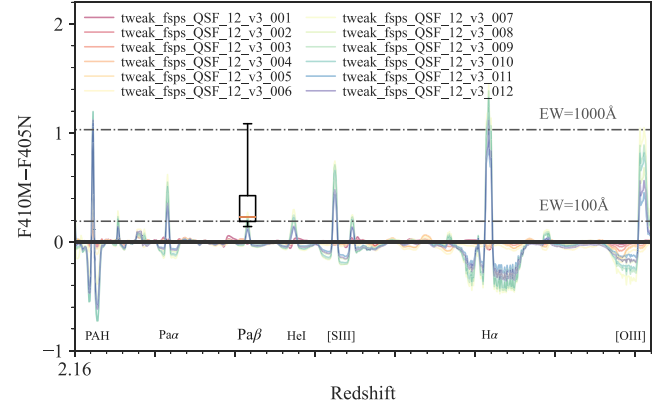
Figure 7. Emission-line contributions to the NB magnitude (F410M−F405N) depending on galaxy redshifts. The box plot shows the 25–75th percentiles of those 17 PBEs confirmed with HAE counterparts and its error bar depicts the whole range. Colored lines indicate the color term values of twelve model templates of star-forming and quiescent galaxies (tweak_fsps_QSF_12_v3, see legends and text) from EAZY (G. B. Brammer et al. 2008). Strong emission lines are appended in the figure; however, it should be noted that the emission-line models are limited and do not comprehensively reproduce NB excesses (see text).

galaxies and AGNs, although quiescent galaxies with small PAH features at $z = 0.2$ may also appear in the NB selection. Moreover, it indicates that the general color term between the F405N and F410M filters is negligible because the offset in their center wavelengths is small (0.037 μm, Figure 1).

In light of these trends, we apply a color–color selection based on the obtained medium and broadband images (F115W −F182M versus F182M−F410M), excluding foreground and background contaminants on a best-effort basis. Figure 8 shows NBEs (Section 3.1) on the color–color diagram on the left side, and the expected locations of line emitters at various redshifts possibly chosen by NB selection on the right side. We correct Galactic extinction by assuming the dust reddening value of E $(B - V) = 0.0336$ (E. F. Schlafly & D. P. Finkbeiner 2011) and following the J. A. Cardelli et al. (1989) extinction curve. On the right panel of Figure 8, we adopt model templates at $z_{center} \pm 0.1$ from EAZY (G. B. Brammer et al. 2008), but only those of star-forming galaxies except for the PAH $\lambda3.3\,\mu$m line at $z = 0.2$ (see discussion above), where z_{center} indicates the emission-line redshift caught by the center wavelength of the F405N NB filter. Figure 8 also demonstrates that the color distributions of the model templates at $z = 2.2$ are consistent with those of known protocluster members (HAEs) at the same redshift.

Based on the known HAEs and model templates, we set the following color thresholds (see also Figure 8),
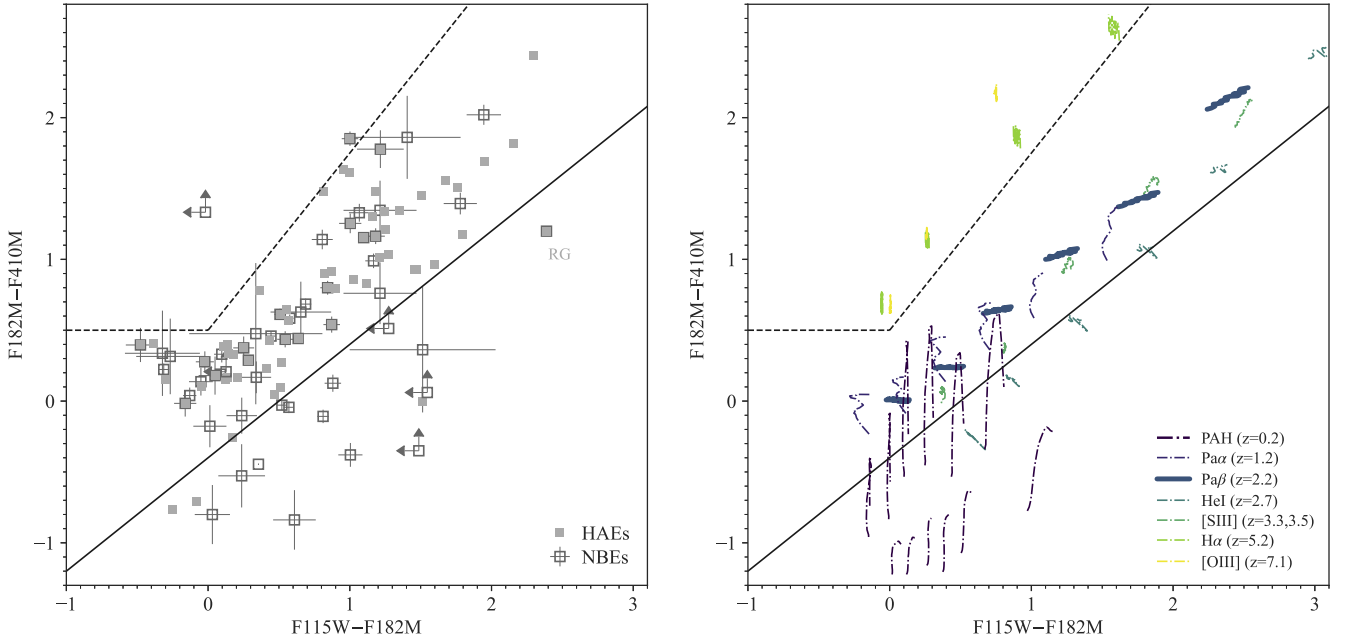
$$F182M - F410M > 0.8(F115W - F182M) - 0.4, \quad (7)$$

and

$$F182M - F410M < 0.5, \quad \text{or} \quad (8)$$

$$F182M - F410M < 1.25(F115W - F182M) + 0.5. \quad (9)$$

These color criteria enclose most of the NIRCam sources with HAE counterparts within $0''5$ (63 out of 65 with duplicates) and 39 out of 57 NBEs. Additionally, we include two omitted NBEs in the final PBE candidates because they have HAE counterparts (Figure 8). One should note that two NBEs without F115W and F182M detection are not shown in the figure and are also removed from the PBE candidates. However, as inferred from the SED templates, completely removing potential foreground/

Figure 8. Color–color diagram (F115W−F182M vs. F182M−F410M) for NBEs on the left panel and model templates on the right panel. Open and filled squares on the left show NBEs and known HAEs within the field of view (R. Shimakawa et al. 2024a, Table A), respectively. All colors are based on fixed aperture photometry of $0''.3$ diameter and error bars are calculated from 1σ photometric uncertainties. The black solid and dashed lines indicate the color thresholds adopted in this work to select PBE candidates at $z = 2.2$. On the right panel, colored curves depict the model colors based on SED templates from EAZY (G. B. Brammer et al. 2008): all 12 templates for PAH $\lambda 3.3$ μm line at $z = 0.23 \pm 0.10$ in purple, and 6 templates of star-forming galaxies for the other line emitters (dark blue: Paα at $z = 1.17 \pm 0.10$, blue: Paβ at $z = 2.17 \pm 0.10$, cyan: HeI at $z = 2.74 \pm 0.10$, green: [S III] at $z = 3.36 \pm 0.20$, yellow-green: Hα at $z = 5.18 \pm 0.10$, and yellow: [O III] at $z = 7.10 \pm 0.10$).

background contaminants is challenging with only two color information because the color distribution of PBEs largely overlaps with those of some foreground/background emitters, particularly $z = 0.2$ PAH, $z = 1.2$ Paα, and $z = 3.4$ [S III] emitters (Figure 8). Meanwhile, we cannot rule out the possibility that excluded sources, especially those without F182M detection at the lower right of the figure, could be PBEs. Besides, the color–color diagram suggests the detection of an HAE at $z = 5.2$ or [O III] emitter at $z \sim 7.1$, showing a significantly redder F182M−F410M color than the other NBEs for a given F115W−F182M color. However, if we apply the recent measurement of Hα luminosity at $z = 6$ (F. Sun et al. 2023, Figure 8) to the survey field, it is estimated that ~ 6 Hα emitters may be detected. Furthermore, Wold et al. (2024, Figure 13) have constrained [O III] luminosity function at $z = 7$, suggesting that we may find 0–2 [O III] emitters. Thus, as only one candidate in the background is lower than what we roughly expected, there could be some background emitters that have not yet been removed from the PBE candidates.

3.3. Emitter Catalog

Based on our analyses, we select 57 NBEs using NB selection and exclude 16 NBEs via color–color selection from PBE candidates (Section 3.2). Thus, we have narrowed the original NBE samples down to 41 PBE candidates likely to be associated with the Spiderweb protocluster at $z = 2.16$, which meet the following selection criteria:

$$\mathrm{ID}_{S18} \neq \varnothing, \quad \text{or} \tag{10}$$

$$\mathrm{Flag}_{color} = 1, \tag{11}$$

Table 1
List of NBE Samples (Section 3.3)

ID	ID_{S18}	Flag_{color}	F_{NB} (10^{-18} erg s^{-1} cm^{-2})	$\mathrm{EW}_{z=2.16}$ (Å)
1	⋯	1	16.0 ± 2.7	145 ± 7
2	⋯	1	11.5 ± 4.7	160 ± 17
3	⋯	1	3.0 ± 2.1	68 ± 22
			⋯	

(This table is available in its entirety in machine-readable form in the online article.)

where ID_{S18} is the identification number of the HAE counterparts in R. Shimakawa et al. (2018b, 2024a), and Flag_{color} is the color selection flag in Section 3.2. The color selection flag denotes $\mathrm{Flag}_{color} = 1$ if the F115W−F182M and F182M−F410M colors fit the selection criteria (Equations (7)–(9)).

The object identification numbers, color selection flags, line fluxes, and the rest-frame EWs at $z = 2.16$ ($\mathrm{EW}_{z=2.16}$) for all 57 NBEs are summarized in Table 1. We estimate the total NB fluxes and $\mathrm{EW}_{z=2.16}$ for individual NBEs via the following prescription:

$$F_{\mathrm{NB}} = \frac{\Delta_{\mathrm{NB}}(f_{\mathrm{NB}} - f_{\mathrm{BB}})}{1 - \Delta_{\mathrm{NB}}/\Delta_{\mathrm{BB}}}, \tag{12}$$

$$\mathrm{EW}_{z=2.16} = \frac{\Delta_{\mathrm{NB}}(f_{\mathrm{NB}} - f_{\mathrm{BB}})}{f_{\mathrm{BB}} - f_{\mathrm{NB}} \cdot \Delta_{\mathrm{NB}}/\Delta_{\mathrm{BB}}} \frac{1}{3.16}, \tag{13}$$

where Δ is the filter bandwidth ($\Delta_{\mathrm{NB}} = 460$ Å and $\Delta_{\mathrm{BB}} = 4360$ Å). The total flux densities in the F405N (f_{NB}) and F410M (f_{BB}) bands are based on MAG_AUTO photometry

in the SEXTRACTOR (E. Bertin & S. Arnouts 1996), and their photometric errors are calculated via Equations (3)–(4). We do not consider potential filter loss due to the small difference between the two filter throughputs since most Paβ line wavelengths of HAEs with spectroscopic redshifts are well covered by the N405N filter.

4. Discussion

4.1. Spatial Distribution

The spatial distribution of 41 PBE candidates and 58 known HAEs around the Spiderweb radio galaxy is shown in Figure 9; both samples are plotted on the RGB color image (F410M/F182M/F115W) covered by the JWST/NIRCam imaging. Notably, many of the known HAE samples (41/58) are not selected as PBEs owing to the selection effects discussed in Section 3.1. Therefore, we observe an apparent segregation between HAEs and PBE candidates in spatial distributions on the local scale. The small offset of redshift coverage by Hα and Paβ NB filters is another causal factor of the difference in spatial distribution. However, their distribution patterns are broadly consistent with each other; both populations spread toward the east and west from the center, while only a few galaxies are located in the northern and southern areas (Figure 9). Some PBE candidates without HAE counterparts (#10, 17, 20, 32, 37 and #38, 49, 61 outside of the Hα imaging) could form a substructure in the southern region or the bottom part of Figure 9, where no HAE have been detected in Y. Koyama et al. (2013a) and R. Shimakawa et al. (2018b). They could trace a backward structure at $z \sim 2.18$ in the Spiderweb protocluster undetectable by the Hα NB filter (at $z > 2.175$; Figure 1). However, we cannot rule out the possibility of projection effects due to non-Paβ emitters in the foregrounds and/or backgrounds.

We now focus more on some individual PBE candidates. Figure 9 shows two new member candidates (#31 and #35) within an r_{500} radius of 220 proper kiloparsecs (P. Tozzi et al. 2022a). #31 is a faint source that is marginally detected in the NIRCam images but invisible in the currently available ground-based data. We consider that #35 might have been missed in previous Hα imaging (J. D. Kurk et al. 2004b; Y. Koyama et al. 2013a; R. Shimakawa et al. 2018b) because it was disturbed by a nearby bright object at a distance of 1″3 in the seeing-limited NB image. Notably, another new candidate deblended by the NIRCam high-resolution images is observed (#26 located 1″ from a brighter source). Conversely, as summarized in Table 1, #5, 6, 12, 14, 16, 27, 28, 29, 30, 34, 40, 46, 52, 54, 56, 57, 66 have HAE counterparts in R. Shimakawa et al. (2018b); hence, they are so-called dual Hα + Paβ emitters. Their emission-line ratios and environmental dependence are discussed by J. M. Pérez-Martínez et al. (2024). Cross-matching with other populations, such as quiescent galaxies and submillimeter sources, and detailed analyses of their physical properties are left to future studies.

4.2. Line Luminosity Function

The line luminosity function gives fundamental information regarding galaxy abundance as a function of the luminosity (D. Sobral et al. 2010, 2011, 2013, 2015; M. Hayes et al. 2010; C. Ly et al. 2011; J. Matthee et al. 2017; M. Hayashi et al. 2018, 2020; R. Shimakawa et al. 2018a; X. Z. Zheng et al. 2021; G. Nagaraj et al. 2023). This section estimates the Paβ

line luminosity function based on the selected PBE candidates. The number excess of massive star-forming galaxies (or AGNs) in the Spiderweb protocluster compared to the general field has been reported in previous studies (N. A. Hatch et al. 2011; Y. Koyama et al. 2013a, 2013b; R. Shimakawa et al. 2018b), which would enhance the line luminosity function at the bright end. In contrast, NB selection only selects Paβ emitters with high EWs (>20 Å) and misses massive galaxies, as explained in Section 3.1, which would suppress the number density at the bright end.

We calculate the number densities per unit Paβ luminosity following the $V_{\max}$ procedure,

$$\phi_{\text{obs}}(\log L) = \sum_i \frac{1}{V_{\max} C \Delta(\log L)}, \qquad (14)$$

where $V_{\max}$ is the survey volume ($=1812$ co-Mpc^3) of the NIRCam Paβ NB imaging (Figure 2), and C is the selection completeness obtained through the Monte Carlo simulation (Section 3.1). The survey volume is determined from the survey area (20.90 arcmin^2 or 53.91 co-Mpc^2) and the filter width of the F405N NB filter (0.046 μm or 33.61 co-Mpc). We do not apply the completeness correction to the bright-end sources at F405N < 22 mag (applying to only the radio galaxy) since the simulated completeness value for typical NBEs is nearly zero (Figure 6). Notably, dust attenuation is not considered in this work because it is discussed in the companion study (J. M. Pérez-Martínez et al. 2024), and PBE candidates are not fully covered by the previous Hα NB imaging (Figure 2). Given the limited sample size, we adopt a relatively large bin size of $\Delta(\log L) = 0.2$.

The resultant Paβ luminosity function is shown in Figure 10. The luminosity function can be formed by a Schechter function (P. Schechter 1976, $\phi(L)$), given by the following equation:

$$\phi(L) d(\log L) = \phi^* \left(\frac{L}{L^*}\right)^{\alpha+1} \exp\left(-\frac{L}{L^*}\right) \ln 10 \, d(\log L). \quad (15)$$

This is a logarithmic expression transformed from the original formula. ϕ^*, L^*, and α are Schechter parameters, where ϕ^* is a normalization density at a characteristic luminosity L^*, and α is a scaling exponent of the power law driving the luminosity function at the faint end ($L \ll L^*$). We perform a chi-square fitting to the $\phi_{\text{obs}}(\log L)$ values (Equation (14)) above the luminosity threshold of $L_{\text{H}\alpha,\text{corr}} = 10^{40.9}$ erg s^{-1} using a fitting algorithm, LMFIT (M. Newville et al. 2023, version 1.2.1). We do not consider luminosity bins below $\log(L_{\text{Pa}\beta}/\text{erg s}^{-1}) = 40.9$ (F405N ~ 25 mag) during curve fitting because we cannot well recover the number densities due to the severe lack of the selection completeness below $\sim 50\%$ (Figure 6). Consequently, we obtain the best-fit parameters $\log \phi^* = -2.53 \pm 0.15$ and $\log L^* = 42.33 \pm 0.17$, as indicated in Figure 10. Here, given the limited sample size, the scaling exponent is fixed to $\alpha = -1.6$ according to the studies by D. Sobral et al. (2013) and M. Hayashi et al. (2018), which reported that the faint-end slope is reasonably fitted by $\alpha = -1.6$ regardless of the redshift at least up to $z \sim 2.2$. We confirm that the fitting result is not significantly improved even if we choose different α values. The effects of stellar absorption are ignored, assuming they are sufficiently small throughout the study (e.g., EW $\lesssim 1$–2 Å in absorption according to A. Calabrò et al. 2019; L. M. Seillé et al.
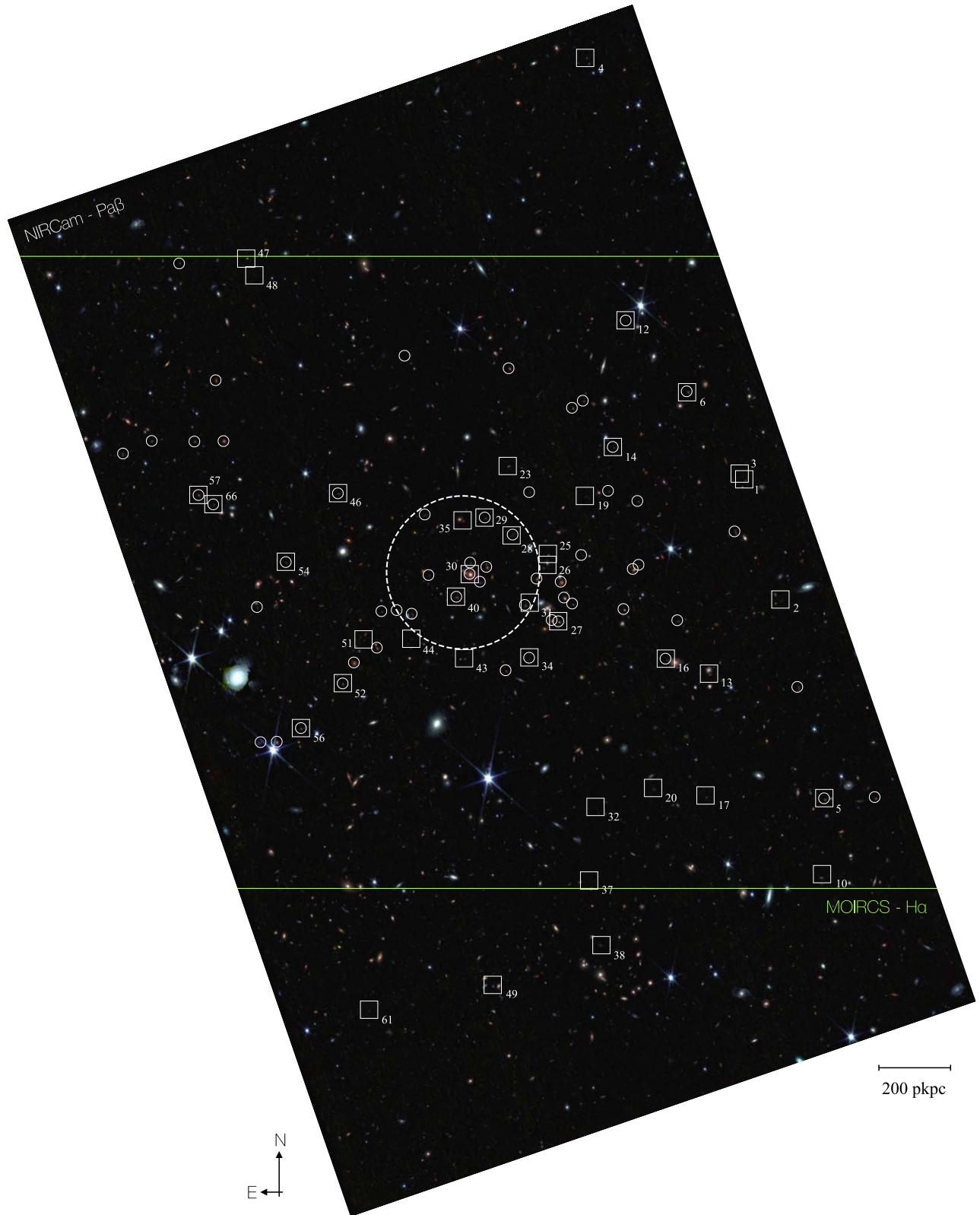
Figure 9. Spatial distribution of PBE candidates (squares) and known HAEs (circles; R. Shimakawa et al. 2024a, Table A) around the Spiderweb radio galaxy on the RGB (F410M/F182M/F115W) image made by STIFF (E. Bertin 2012). We here plot PBE candidates that satisfy the selection criteria (Equations (10)–(11)). The green lines depict the survey area of the Hα line imaging. The dashed circle indicates the virial radius ($r_{500} = 220$ proper kpc) based on the X-ray measurement by P. Tozzi et al. (2022a).

2024), owing to the lack of observational constraints. Moreover, the nontophat transmittance profile of the F405N NB filter could affect the shape of the Paβ luminosity function at the bright end

(D. Sobral et al. 2013; R. Shimakawa et al. 2018a). However, as we have not been able to constrain the bright-end densities of PBEs, we do not consider such an effect.
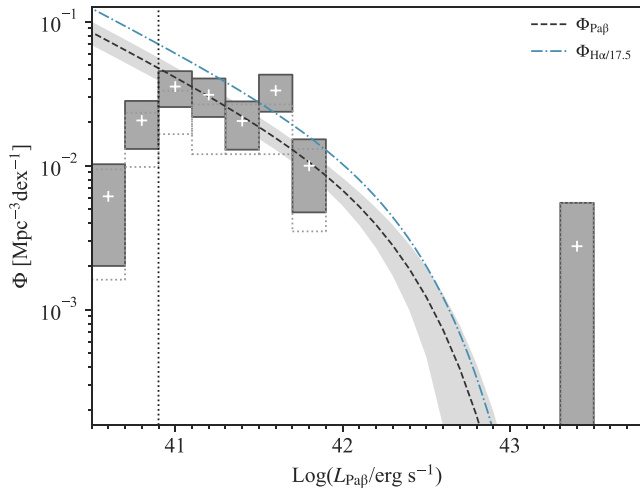
Figure 10. Paβ luminosity function for the selected PBE candidates in the Spiderweb protocluster at $z = 2.16$. The gray-filled and open dotted squares show the number densities in each Paβ luminosity bin with and without the completeness correction (Section 3.1), respectively. The best-fit Paβ luminosity function is depicted by the black dashed curve with a 1σ error range in gray, where the density bins below the threshold marked by the dotted vertical line are not taken into account. The blue dashed–dotted curve is the dust-corrected Hα luminosity function for the HAE sample reported by R. Shimakawa et al. (2018b), including a scaling factor of Hα/Pa $\beta = 17.5$.

The best-fit Paβ luminosity function of the PBE candidates is 1.5 times lower than the dust-corrected Hα luminosity function by R. Shimakawa et al. (2018b) assuming the Hα/Paβ line ratio of 17.5. The differential is presumably due to the selection bias in the NB selection, given the significant fraction of unmatched samples between PBE candidates and HAEs. In particular, no Paβ-luminous emitters with $L_{Pa\beta} > 10^{42}$ erg s^{-1} are detected, with the exception of the Spiderweb radio galaxy (#30). The different survey areas (Figure 2) also contribute to the difference since the Hα imaging is more optimized to dense substructures in the protocluster. In addition, the dust extinction would have a minor effect, which increases the Paβ luminosity by 0.13 dex when assuming Paβ extinction of 0.33 mag (or $A_{H\alpha} = 1$; J. M. Pérez-Martínez et al. 2024). Besides, R. Shimakawa et al. (2018b) reported an overdensity of $\delta = 12.29$ in the Hα luminosity function when compared to that in the general field (D. Sobral et al. 2014). From these comparisons, a number excess of the obtained Paβ luminosity function is tentatively estimated to be $\delta \sim 8$. However, one should note that the current Paβ luminosity function needs to be considered as an upper limit because it would contain other line emitters at $z \neq 2.2$ (Section 3.2).

4.3. Possible Emitters Seen Only in the Narrowband

Finally, we discuss the possibility of missing faint emitters visible only in the F405N image, hereafter referred to as NB-only emitters. Since we use the median-stacked image of all four band filters for source detection (Section 2.2), we could overlook emission-line-dominated emitters that are too faint to be detected in the F115W/F182M/F410M bands and, hence, in the median combined image. Such peculiar sources have been observed commonly in the NB imaging survey (e.g., M. Hayashi et al. 2016; T. Shibuya et al. 2018). Although their characteristics largely depend on the limiting magnitudes of the observing bands and their combination, they generally tend to be low-mass star-forming galaxies with high specific star formation rates (e.g., M. Hayashi et al. 2016) like extreme emission-line galaxies (C. Cardamone et al. 2009;
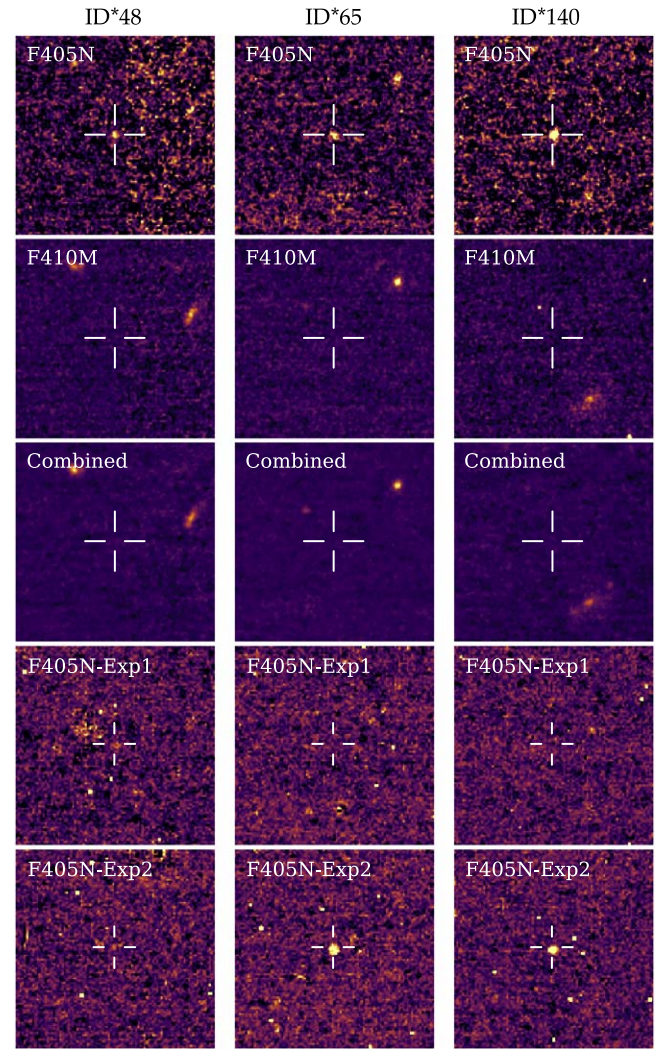
Figure 11. Example cutouts of NB-only emitters that are not used in this study. The first, second, and third rows show them on the F405N, F410M, and four-band combined images, respectively. They are normalized with a linear stretch in the same flux range. The fourth and fifth rows show individual exposures in the F405N band for each source, which are normalized in a different range to the first-to-third rows for the sake of visibility. For the two sources on the right and middle panels, cosmic rays are detected in one of the exposures.

R. O. Amorín et al. 2010; Y. I. Izotov et al. 2012; T. Kojima et al. 2020).

Therefore, we rerun the NB selection as in Section 3.1, but we adopt the F405N image as the detection image instead of the combined image. Here, we modify a parameter of DETECT_MINAREA =15 and add a Gaussian filter of Gauss_3.0_5x5 to capture very faint objects, although these parameter changes significantly increase false detection. Then, we select additional NBE candidates satisfying the selection criteria (Equations (5)–(6)) from the undetected samples in the F410M band above two sigma levels, amounting to 138 sources. In the end, however, only 26 candidates remain after a careful visual inspection. The excluded samples comprise obvious artifacts due to cosmic rays with one or a few bright pixels. Figure 11 shows some examples of the screened sources, including how they are present only in the F405N image and not detected in the F410M and combined images.
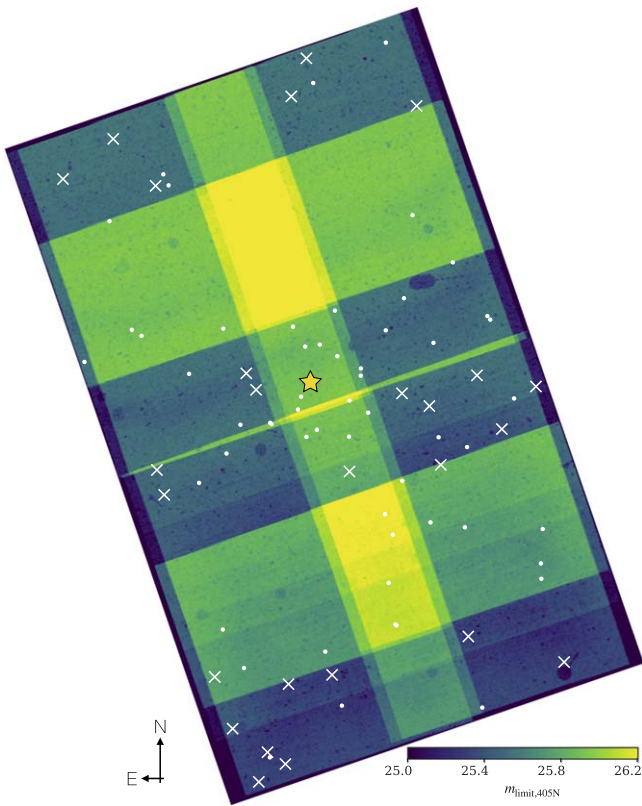
Figure 12. Spatial distribution of NBE candidates with only the NB detection (white crosses). The color map in the background shows the depth in the F405N band as shown in Figure 2. They tend to be located in the shallowest field with the number of exposures $N_{exp} = 2$. The small white circles are NBEs selected in the main analysis (Section 3.1). The yellow star is the Spiderweb radio galaxy.

We examine their spatial distribution on the weight map in the F405N band for further validation, as shown in Figure 12. Notably, most candidates of NB-only emitters are distributed in areas of a small number of exposures (corresponding to lower weight values), making the credibility of these detections highly questionable. As these shallow areas comprise only two integrations, some artifacts most likely remain owing to the inability to measure the median values when combining the images. In fact, we confirm that 88% (23/26) of them are most likely surviving cosmic rays by checking individual exposures as illustrated in Figure 11. Although the remaining three sources could be real objects, they can be explained by a result of random variation in the three sigma threshold in our NB selection (Equation (5)) as the total number of source detection used here is ∼2700. Considering the results of these validation checks, we decide not to include these emitter candidates in the main targets, and mention them in this last section instead of the main text.

5. Conclusions

We present our initial results on Paβ line imaging with JWST/NIRCam toward one of the best-studied protoclusters known as the Spiderweb protocluster at $z = 2.16$ (C. L. Carilli et al. 1997; L. Pentericci et al. 1997, 2000; J. D. Kurk et al. 2000). To maximize the science outputs, we focus on the NB F405N and medium-band F410M imaging, and in parallel, the F115W and F182M imaging on the blue channel, allowing us

to obtain Paβ line and the rest-frame *UVJ* colors of protocluster members across the survey field. This paper summarizes the NB technique and color–color selection to find candidates of PBEs as one of the first reports in the series. Then, we investigate the Paβ luminosity function by correcting the selection completeness.

The research highlights of this study are described as follows. We first conduct NB selection on the color–magnitude diagram (F410M−F405N versus F405N) to select NBEs. Consequently, we obtain 57 NBEs showing flux excesses in the F405N band above three sigma levels ($\Sigma > 3$). Subsequent color–color selection (F182M−F410M versus F115W −F182M) helps us remove potential foreground or background contaminants, such as PAH $\lambda 3.3$ μm at $z = 0.2$ and Hα emitters at $z = 5.2$, further narrowing the PBE candidates down to 41 sources. As 17 of the PBE candidates are also confirmed as Hα emitters based on the previous Hα imaging (R. Shimakawa et al. 2018b), the remaining 24 objects are considered to be unconfirmed candidates associated with the Spiderweb protocluster. These PBE candidates are still at risk of foreground or background emitters other than PBEs; therefore, further follow-up studies are needed to establish that they are protocluster members. Additionally, one Hα or [O III] emitter candidate at $z > 5$ is obtained via the selection process.

The original goal of this study was to make a deep line survey aimed at PBEs with a unique NB filter on JWST/ NIRCam, taking advantage of NIR observation less sensitive to dust extinction. In fact, we have succeeded in finding new candidates for protocluster members. However, the general NB technique requires a relatively high EW threshold, which makes it difficult to select bright (and dust-obscured) PBEs as demonstrated in this study. In terms of achieving a more unbiased search of NIR lines with low EWs ($\lesssim$20 Å), wide-field slitless spectroscopy would be more suitable than NB imaging.

The final PBE candidates selected in this study show a similar spatial distribution of HAEs, as established in the previous studies (Y. Koyama et al. 2013a; R. Shimakawa et al. 2018b). We then investigate the Paβ luminosity function for the PBE candidates by measuring their Paβ fluxes based on the newly obtained JWST/NIRCam imaging data. The characteristic Paβ luminosity and normalization density are estimated to be $\log L^* = 42.33 \pm 0.17$ and $\log \phi^* = -2.53 \pm 0.15$, respectively. Follow-up confirmations and characterizations of the PBE candidates will provide a better understanding of the total star formation rate in the Spiderweb protocluster, the environmental dependence of galaxy formation, and a transition process from a protocluster to a bona fide cluster of galaxies.

ORCID iDs

Rhythm Shimakawa ⓘ https://orcid.org/0000-0003-4442-2750
J. M. Pérez-Martínez ⓘ https://orcid.org/0000-0002-5963-6850
Helmut Dannerbauer ⓘ https://orcid.org/0000-0001-7147-3575
Yusei Koyama ⓘ https://orcid.org/0000-0002-0479-3699
Tadayuki Kodama ⓘ https://orcid.org/0000-0002-2993-1576
Pablo G. Pérez-González ⓘ https://orcid.org/0000-0003-4528-5639
Yuheng Zhang ⓘ https://orcid.org/0000-0001-5757-5719
Abdurrahman Naufal ⓘ https://orcid.org/0000-0001-7713-0434
Kazuki Daikuhara ⓘ https://orcid.org/0000-0002-9509-2774

References

Alonso-Herrero, A., Rieke, G. H., Rieke, M. J., et al. 2006, ApJ, 650, 835
Amorín, R. O., Pérez-Montero, E., & Vílchez, J. M. 2010, ApJL, 715, L128
Astropy Collaboration, Price-Whelan, A. M., Sipőcz, B. M., et al. 2018, AJ, 156, 123
Astropy Collaboration, Robitaille, T. P., Tollerud, E. J., et al. 2013, A&A, 558, A33
Bagley, M. B., Finkelstein, S. L., Koekemoer, A. M., et al. 2023, ApJL, 946, L12
Bertin, E. 2012, in ASP Conf. Ser. 461, Astronomical Data Analysis Software and Systems XXI, ed. P. Ballester, D. Egret, & N. P. F. Lorente (San Francisco, CA: ASP), 263
Bertin, E., & Arnouts, S. 1996, A&AS, 117, 393
Bolton, J. G., Savage, A., & Wright, A. E. 1979, AuJPA, 46, 1
Bradley, L., Sipőcz, B., Robitaille, T., et al. 2023, astropy/photutils: v1.10.0, Zenodo, doi:10.5281/zenodo.1035865

Brammer, G. B., van Dokkum, P. G., & Coppi, P. 2008, ApJ, 686, 1503
Bunker, A. J., Warren, S. J., Hewett, P. C., & Clements, D. L. 1995, MNRAS, 273, 513
Bushouse, H., Eisenhamer, J., Dencheva, N., et al. 2023, JWST Calibration Pipeline, v1.10.2, Zenodo, doi:10.5281/zenodo.7829329
Calabrò, A., Daddi, E., Puglisi, A., et al. 2019, A&A, 623, A64
Calzetti, D., Kennicutt, R. C., Engelbracht, C. W., et al. 2007, ApJ, 666, 870
Cardamone, C., Schawinski, K., Sarzi, M., et al. 2009, MNRAS, 399, 1191
Cardelli, J. A., Clayton, G. C., & Mathis, J. S. 1989, ApJ, 345, 245
Carilli, C. L., Röttgering, H. J. A., van Ojik, R., Miley, G. K., & van Breugel, W. J. M. 1997, ApJS, 109, 1
Carilli, C. L., & Walter, F. 2013, ARA&A, 51, 105
Chabrier, G. 2003, PASP, 115, 763
Chaudhuri, A., Majumdar, S., & Nath, B. B. 2013, ApJ, 776, 84
Conroy, C. 2013, ARA&A, 51, 393
Croft, S., Kurk, J., van Breugel, W., et al. 2005, AJ, 130, 867
Dekel, A., Birnboim, Y., Engel, G., et al. 2009, Natur, 457, 451
Di Mascolo, L., Saro, A., Mroczkowski, T., et al. 2023, Natur, 615, 809
Doherty, M., Tanaka, M., De Breuck, C., et al. 2010, A&A, 509, A83
Förster Schreiber, N. M., & Wuyts, S. 2020, ARA&A, 58, 661
Gimenez-Arteaga, C., Brammer, G. B., Marchesini, D., et al. 2022, ApJS, 263, 17
Harris, C. R., Millman, K. J., van der Walt, S. J., et al. 2020, Natur, 585, 357
Hatch, N. A., Kurk, J. D., Pentericci, L., et al. 2011, MNRAS, 415, 2993
Hayashi, M., Kodama, T., Koyama, Y., et al. 2010, MNRAS, 402, 1980
Hayashi, M., Kodama, T., Tanaka, I., et al. 2016, ApJL, 826, L28
Hayashi, M., Shimakawa, R., Tanaka, M., et al. 2020, PASJ, 72, 86
Hayashi, M., Tanaka, M., Shimakawa, R., et al. 2018, PASJ, 70, S17
Hayes, M., Schaerer, D., & Östlin, G. 2010, A&A, 509, L5
Hinshaw, G., Larson, D., Komatsu, E., et al. 2013, ApJS, 208, 19
Hunter, J. D. 2007, CSE, 9, 90
Ichikawa, T., Suzuki, R., Tokoku, C., et al. 2006, Proc. SPIE, 6269, 626916
Iqbal, A., Majumdar, S., Nath, B. B., et al. 2017, MNRAS, 472, 713
Izotov, Y. I., Thuan, T. X., & Guseva, N. G. 2012, A&A, 546, A122
Jin, S., Dannerbauer, H., Emonts, B., et al. 2021, A&A, 652, A11
Kennicutt, R. C. J. 1998, ApJ, 498, 541
Kojima, T., Ouchi, M., Rauch, M., et al. 2020, ApJ, 898, 142
Kooistra, R., Inoue, S., Lee, K.-G., et al. 2022, ApJ, 927, 53
Koyama, Y., Kodama, T., Kodama, K.-I., et al. 2013a, MNRAS, 428, 1551
Koyama, Y., Smail, I., Kurk, J., et al. 2013b, MNRAS, 434, 423
Kurk, J. D., Pentericci, L., Overzier, R. A., et al. 2004a, A&A, 428, 817
Kurk, J. D., Pentericci, L., Röttgering, H. J. A., et al. 2004b, A&A, 428, 793
Kurk, J. D., Röttgering, H. J. A., Pentericci, L., et al. 2000, A&A, 358, L1
Lepore, M., Di Mascolo, L., Tozzi, P., et al. 2024, A&A, 682, A186
Lilly, S. J., Eales, S. A., Gear, W. K. P., et al. 1999, ApJ, 518, 641
Luridiana, V., Morisset, C., & Shaw, R. A. 2015, A&A, 573, A42
Ly, C., Lee, J. C., Dale, D. A., et al. 2011, ApJ, 726, 109
Madau, P., Pozzetti, L., & Dickinson, M. 1998, ApJ, 498, 106
Matthee, J., Sobral, D., Best, P., et al. 2017, MNRAS, 471, 629
Miley, G. K., Overzier, R. A., Zirm, A. W., et al. 2006, ApJL, 650, L29
Nagaraj, G., Ciardullo, R., Bowman, W. P., et al. 2023, ApJ, 943, 5
Neufeld, C., van Dokkum, P., Asali, Y., et al. 2024, ApJ, 972, 156
Newville, M., Otten, R., Nelson, A., et al. 2023, lmfit/lmfit-py: v1.2.1, Zenodo, doi:10.5281/zenodo.7887568
Oke, J. B., & Gunn, J. E. 1983, ApJ, 266, 713
Papovich, C., Rudnick, G., Rigby, J. R., et al. 2009, ApJ, 704, 1506
Pentericci, L., Kurk, J. D., Röttgering, H. J. A., et al. 2000, A&A, 361, L25
Pentericci, L., Roettgering, H. J. A., Miley, G. K., et al. 1997, A&A, 326, 580
Pérez-González, P. G., Barro, G., Rieke, G. H., et al. 2024, ApJ, 968, 4
Pérez-Martínez, J. M., Dannerbauer, H., Kodama, T., et al. 2023, MNRAS, 518, 1707
Pérez-Martínez, J. M., Dannerbauer, H., Koyama, Y., et al. 2024, ApJ, 977 74
Pontoppidan, K. M., Pickering, T. E., Laidler, V. G., et al. 2016, Proc. SPIE, 9910, 991016
Pratt, G. W., Arnaud, M., Piffaretti, R., et al. 2010, A&A, 511, A85
Reback, J., Jbrockmendel, W. J., McKinney, W., et al. 2022, pandas-dev/ pandas: Pandas v1.4.3, Zenodo, doi:10.5281/zenodo.6702671
Reddy, N. A., Topping, M. W., Sanders, R. L., et al. 2023, ApJ, 948, 83
Rieke, M. J., Kelly, D., & Horner, S. 2005, Proc. SPIE, 5904, 1
Rinaldi, P., Caputi, K. I., Costantin, L., et al. 2023, ApJ, 952, 143
Roettgering, H. J. A., Lacy, M., Miley, G. K., et al. 1994, A&AS, 108, 79
Roettgering, H. J. A., van Ojik, R., Miley, G. K., et al. 1997, A&A, 326, 505
Schechter, P. 1976, ApJ, 203, 297
Schlafly, E. F., & Finkbeiner, D. P. 2011, ApJ, 737, 103
Seillé, L. M., Buat, V., Fernández, V., et al. 2024, A&A, 689, A102

Shapley, A. E. 2011, ARA&A, 49, 525
Shibuya, T., Ouchi, M., Konno, A., et al. 2018, PASJ, 70, S14
Shimakawa, R., Kodama, T., Hayashi, M., et al. 2018a, MNRAS, 473, 1977
Shimakawa, R., Koyama, Y., Kodama, T., et al. 2024b, arXiv:2410.11174
Shimakawa, R., Koyama, Y., Röttgering, H. J. A., et al. 2018b, MNRAS, 481, 5630
Shimakawa, R., Kodama, T., Tadaki, K. I., et al. 2014, MNRAS, 441, L1
Shimakawa, R., Pérez-Martínez, J. M., Koyama, Y., et al. 2024a, MNRAS, 528, 3679
Sobral, D., Best, P. N., Geach, J. E., et al. 2009, MNRAS, 398, 75
Sobral, D., Best, P. N., Geach, J. E., et al. 2010, MNRAS, 404, 1551
Sobral, D., Best, P. N., Smail, I., et al. 2011, MNRAS, 411, 675
Sobral, D., Best, P. N., Smail, I., et al. 2014, MNRAS, 437, 3516
Sobral, D., Matthee, J., Best, P. N., et al. 2015, MNRAS, 451, 2303
Sobral, D., Smail, I., Best, P. N., et al. 2013, MNRAS, 428, 1128
Stern, J., Fielding, D., Faucher-Giguere, C.-A., & Quataert, E. 2020, MNRAS, 492, 6042

Stevens, J. A., Ivison, R. J., Dunlop, J. S., et al. 2003, Natur, 425, 264
Sun, F., Egami, E., Pirzkal, N., et al. 2023, ApJ, 953, 53
Suresh, J., Nelson, D., Genel, S., Rubin, K. H. R., & Hernquist, L. 2019, MNRAS, 483, 4040
Suzuki, R., Tokoku, C., Ichikawa, T., et al. 2008, PASJ, 60, 1347
Tacconi, L. J., Genzel, R., & Sternberg, A. 2020, ARA&A, 58, 157
Tanaka, M., De Breuck, C., Venemans, B., et al. 2010, A&A, 518, A18
Tanaka, M., Toft, S., Marchesini, D., et al. 2013, ApJ, 772, 113
Taylor, M. B. 2005, in ASP Conf. Ser. 347, Astronomical Data Analysis Software and Systems XIV, ed. P. Shopbell, M. Britton, & R. Ebert (San Francisco, CA: ASP), 29
Tozzi, P., Gilli, R., Liu, A., et al. 2022a, A&A, 667, A134
Tozzi, P., Pentericci, L., Gilli, R., et al. 2022b, A&A, 662, A54
van Ojik, R. 1995, PhD thesis, Univ. Leiden, Netherlands
Wold, I. G. B., Malhotra, S., Rhoads, J. E., et al. 2024, arXiv:2407.19023
Zheng, X. Z., Cai, Z., An, F. X., Fan, X., & Shi, D. D. 2021, MNRAS, 500, 4354